ORIGINAL ARTICLE

Design of a torsional stiffener for a cable-driven hyper-redundant robot composed of gear transmission joints

Ardit Poka[1,2] · Federico Manara[1,2] · Daniele Ludovico[1] · Alessandro Pistone[1] ·
Lorenzo De Mari Casareto Dal Verme[1,3] · Giovanni Berselli[1,2] · Darwin G. Caldwell[1] · Carlo Canali[1]

Abstract

This work describes the advancement in developing a cable-driven gear transmission joint designed as a basic element for a long-reach hyper-redundant robot. Hyper-redundancy allows the robot to perform auxiliary tasks such as obstacle avoidance and joint limits satisfaction. This feature makes hyper-redundant robots particularly useful for performing tasks in confined and hazardous environments and areas that are not reachable by a human operator. The long-reach feature of the robot requires a detailed study of the overall structure and its components. The joint must be capable of transmitting forces and movements over a long distance without losing the precision and accuracy of the end-effector, so it is designed to optimise the robot's performance in terms of stiffness, structural resistance, and functional characteristics. In light of the above considerations, the main focus of this work is to improve the structural performance of the entire robotic system. Consequently, since the most critical component of the robot in terms of torsional deformation is the gear transmission joint, this paper aims to design a torsional stiffener element to reduce its deformation and, thus, an increase of torsional stiffness of the overall robotic system. Tube-shaped and rectangular-shaped stiffener elements, which can fit the joint design satisfying its geometrical constraints, are proposed. A computer-aided engineering approach is implemented to improve the precision of positioning of the end-effector by adding stiffener elements in the joint. Two sensitivity analyses, varying the geometry of the proposed stiffener elements, are performed to evaluate their performance in terms of added mass and displacement reduction.

Keywords Robotics · Torsional stiffening · Cable-driven mechanism

1 Introduction

In the last decades, with the development of service robotics, a whole new set of applications and tasks began to be faced by automated or teleoperated systems and robot [1–3]. One relevant field of application is industrial inspection [4]. When a dangerous or difficult-to-reach area needs to be inspected or maintained, using a robotic system can be a very convenient option [5, 6]. Inspection and maintenance represent a critical economic activity in several sectors, such as energy [7], water supply [7], oil and gas [8], civil engineering and infrastructure [9]. Robotic applications have massive potential to increase productivity and improve safety [10].

Although the need to operate in an unstructured and complex environment, recent advances in hardware design, computation capabilities, and control algorithms paved the way for the design, testing, and deployment of new robots, ranging from legged quadrupeds [11] to drones [12], elephant trunk [13, 14], crawler [15], octopus [16], and snake-like robots [17]. In particular, thanks to their mobility within constrained and hazardous environments, hyper-redundant robots can be used for inspecting and maintaining complex industrial plants. Long-reach cable-driven hyper-redundant manipulators have been widely employed in the field of industrial inspection [18], as well as in the nuclear sector [19, 20]. The cable design keeps the actuators safe from the environmental conditions of the workspace and reduces the weight of the manipulator structure. The kinematic redundancy allows the robot to perform multiple tasks simultaneously, like moving into constrained environments on a specific trajectory and avoiding possible obstacles. In addition, due to the March 2011 accident at Fukushima Dai-

---

Ardit Poka and Federico Manara contributed equally to this work

✉ Ardit Poka
   ardit.poka@iit.it

Extended author information available on the last page of the article

ichi nuclear power plants in Japan, the need to develop a specific long-reach robotic arm for decommissioning nuclear reactors has risen. Some examples are the Fukushima Repair Manipulator [21] and the robotic arm developed by Veolia Nuclear Solutions and Mitsubishi Heavy Industries [22].

All the above-mentioned long-reach robots are based on different designs. However, for all of them, the most crucial needs are to maintain a lightweight, to reduce the actuators' size, increase their payload, and at the same time maintain sufficient stiffness to guarantee an accurate end-effector positioning. Therefore, since all the elements in a robotic system do not equally contribute to the overall stiffening of the structure, a key aspect is to identify which components or interactions between them need to be improved.

This work aims to improve the accuracy in the end-effector positioning of the fully actuated cable-driven hyper-redundant robot presented in [23]. Given that this robot moves at a relatively low speed and acceleration, the inertia effects can be neglected. Then, since it is a long-reach manipulator, the main sources of deformation are the static forces induced by the mass of each module. Gear transmission joints, particularly their intermediate links, are the most affected elements by the deformation due to torsional loads. The most important factors to take into account when studying the stiffness of a mechanical system are [24, 25]: (i) the structural deformations due to load-transmitting components (e.g. links and shafts); (ii) the deformations due to power-transmitting devices (e.g. actuators); and (iii) the deformations due to contacts between components (e.g. surface roughness due to imperfect machining). This work focuses specifically on the torsional deformation of the gear transmission joint. Torsional resistance is a common matter in the automotive industry. Indeed different works studied solutions for the torsional stiffening of the vehicles' frames [26, 27]. When facing such design problems the state of the art is to take advantage of additive manufacturing combined with generative design, to obtain an effective geometry with few construction constraints [28] and relying on rapid prototyping for functional tests [29]. This paper represents a preliminary study of a torsional stiffening solution in a robotic system by developing basic designs as a first step towards a more detailed investigation of the phenomenon and better-refined solutions. To increase the torsional stiffness of the gear transmission joint, two stiffening elements designs, meant to be manufactured using machining, are compared in terms of stiffness increase, added mass, and the displacement of the position of the end-effector.

Section 2 summarises the baseline on which this work is founded. Section 3 describes the critical aspects of the joint and the geometrical constraints that the stiffener elements have to satisfy. Section 4 presents the two proposed stiffener elements and compares their performance. Section 5 draws the conclusion and future works.

2 Baseline: robot concept and joint description

The concept of the fully actuated cable-driven hyper-redundant robot and the design of the gear transmission joint, described in [23], are revisited as a baseline on which this work is founded.

2.1 Robot concept

The robot comprises a chassis in which are mounted all the actuators and a robotic arm composed of five modules. Each module, composed of a gear transmission joint and a link, has one rotational Degree of Freedom (DOF) and is driven by a pair of cables. For the task of positioning the end-effector in the Cartesian space, this is a hyper-redundant robot. The gear transmission joint, described in Sect. 2.2, is a mechanism composed of two revolute joints, of which one is constrained to revolute on the other. Table 1 reports the modified DH parameters of the robot, according to [30], where i_c, with $i = 1, \ldots, 5$, represents the constrained revolute joint of the ith module, while EE indicates the end-effector.

Given this assembly configuration, the robot can achieve 3D motions. A virtual prototype of the robotic system, shown in Fig. 1, has been developed with the parameters reported in Table 2, where m and CoM indicate the mass and the centre of mass position of each joint, respectively.

2.2 Joint description

The robotic system presented in Sect. 2.1 comprises several modules connected in series. Each module, driven by a pair of antagonist cables and moved by a single motor, is composed of a gear transmission joint and a rigid link. The gear transmission joint, whose schematic is shown in Fig. 2, consists of two flanges, input and output ones, connected by an

Table 1 DH parameters of the robot

Joint	a [mm]	α [rad]	d [mm]	θ [deg]
1	0	$\pi/2$	0	$q_{1,1}$
1_c	150	0	0	$q_{2,1}$
2	350	$-\pi/2$	0	$q_{1,2}$
2_c	150	0	0	$q_{2,2}$
3	350	$\pi/2$	0	$q_{1,3}$
3_c	150	0	0	$q_{2,3}$
4	350	$-\pi/2$	0	$q_{1,4}$
4_c	150	0	0	$q_{2,4}$
5	350	$\pi/2$	0	$q_{1,5}$
5_c	150	0	0	$q_{2,5}$
EE	350	0	0	0

Fig. 1 Virtual prototype model of the fully actuated cable-driven hyper-redundant robot
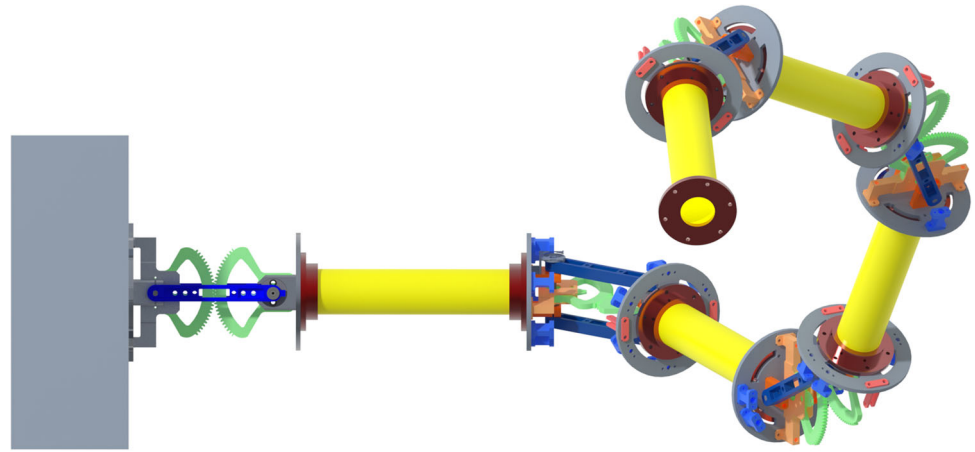
intermediate link of length l_{int} through two revolute joints fixed in O_1 and O_2, respectively.

Two gears, G_1 and G_2, are mounted to the input and output flanges, respectively. This mechanism can be seen as a planetary gear, in which the intermediate link is the carrier and G_2 is the planet that moves around the sun G_1. The reference frame R_0, whose origin and axes are O_0 and x_0-y_0-z_0 respectively, is integral with the input flange. The reference frame R_1, whose origin and axes are O_1 and x_1-y_1-z_1 respectively, is integral with the intermediate link. The reference frame R_2, whose origin and axes are O_2 and x_2-y_2-z_2 respectively, is integral with the output flange. The origins, O_i, and the axes, x_i-y_i-z_i, with $i = 0, \ldots, 2$, are shown in Fig. 2. The two antagonist cables, with lengths l_1 and l_2, are anchored at the points A and B and pass through the points A' and B', respectively. The intermediate link freely rotates around z_1 by an angle θ, while the output flange, integral with G_2, rotates around z_2 by the same angle θ with respect to the intermediate link itself. Consequently, the joint variables $q_{1,j}$ and $q_{2,j}$ are related as follows:

$$q_{1,j} = q_{2,j} = \theta \tag{1}$$

Table 2 Parameters of the robot

Joint	m [kg]	CoM [mm]
1_c	0.465	71
2	2.263	163
2_c	0.474	71
3	2.032	162
3_c	0.472	71
4	1.775	161
4_c	0.234	67
5	1.31	164
5_c	0.219	66
EE	1.16	88

and the total angle produced by the joint is 2θ. Indeed, assuming a gear ratio equal to 1, considering the input flange and G_1 both attached to the reference frame R_0, and exploiting the Willis formulation for planetary gears [31], the overall transmission ratio of the gear transmission joint can be described as follows:

$$\tau = \frac{\omega_{f_{out}}}{\omega_{l_{int}}} = \frac{l_{int}}{r_{G_2}} = 2,$$

where r_{G_2} is the radius of G_2, while $\omega_{f_{out}}$ and $\omega_{l_{int}}$ are the absolute angular velocity of the output flange and the intermediate link, respectively. To respect the design constraints, the joint limits are the following:

$$-q_m \leq q_{1,j} \leq q_m,$$
$$-q_m \leq q_{2,j} \leq q_m,$$

where $q_m = \pi/4$. Defining the actuation coordinate lengths, l_1 and l_2, as follows:

$$l_1 = \left\| A' - A \right\|_2,$$
$$l_2 = \left\| B' - B \right\|_2, \tag{2}$$

it is possible to demonstrate that

$$l_1 + l_2 = 2l_{int} \qquad \forall \theta \in [0, 2\pi). \tag{3}$$

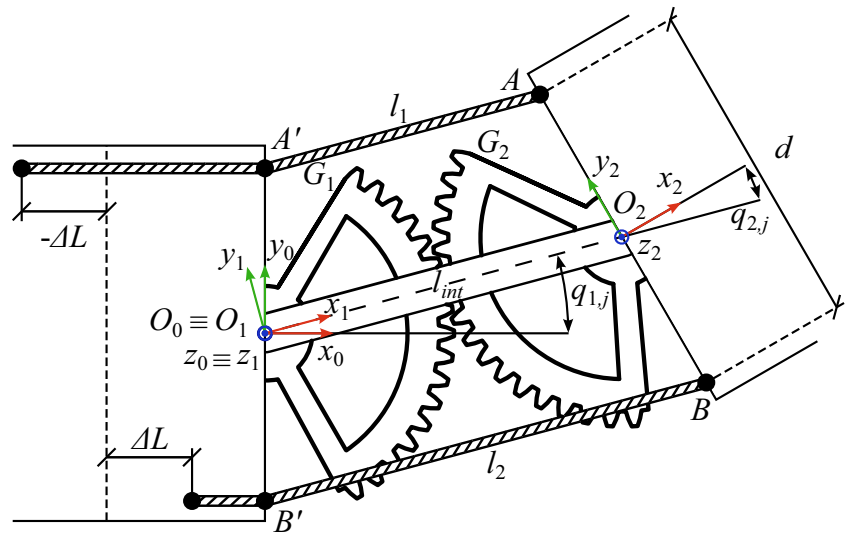For a given joint angle θ, from Eq. 3 follows that the shortening of l_1 and the lengthening of l_2 are equal to:

$$\Delta L = \frac{l_2 - l_1}{2}. \tag{4}$$

Using Eqs. 1 and 4, the direct kinematics, which relates the angle θ and the actuation coordinates in terms of ΔL, is

$$\theta = \text{atan2}\left(\Delta L, \sqrt{d^2 - \Delta L^2}\right), \tag{5}$$

Fig. 2 Gear transmission joint schematic

where

$$d = \|A - B\|_2 = \|A' - B'\|_2.$$

The corresponding inverse kinematics can be computed as follows:

$$\Delta L = d \sin\theta. \tag{6}$$

Using Eqs. 4 and 6, the actuation coordinates can be derived as follows:

$$l_1 = l_{int} - d \sin\theta, \tag{7}$$
$$l_2 = l_{int} + d \sin\theta. \tag{8}$$

3 Problem description

A statistical analysis has been performed to evaluate the maximum torsional load, M_t, applied on the origin O_2 along the x_2-axis of the first joint to obtain a more realistic scenario. First, to make the torsional phenomenon predominant, the joint variables of the first joint have been set to zero, $q_{1,1} = q_{1,2} = 0$. Then, the joint configuration space of the remaining joints was explored using the Latin Hypercube Sampling method since it uniformly divides a given space into a fixed number of hypercubes of equal size, picking a random point in each hypercube. To obtain a statistically representative sample of the joint configuration space, 160, 000 samples have been computed. Next, for each configuration of the robot, the reaction forces and torques for each joint are evaluated, following the static model described in [23], using the parameters listed in Table 2. The distribution of torsional load applied on the origin O_2 along the x_2-axis of the first joint is reported in Fig. 3.

According to this analysis, M_t is obtained when the values of $q_{i,j}$ are zeros for all j except for $j = 2$:

$$q_{1,2} = -\frac{\pi}{4} \text{ rad,}$$
$$q_{2,2} = -\frac{\pi}{4} \text{ rad.}$$

Such configuration is schematised in Fig. 4. The corresponding load value is $M_t = 100$ Nm.

The resulting torsional deformation of the first joint, which can be evaluated through finite element analysis, induces an error on the position of the end-effector of the robot. The structural static analyses performed in this work are executed using PTC Creo® 9.0 and are based on the following assumptions and parameters:
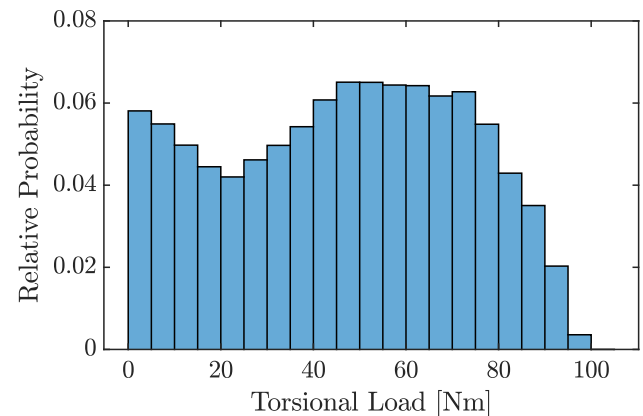
Fig. 3 Torsional load M_t for the first joint as the result of the static numerical analysis
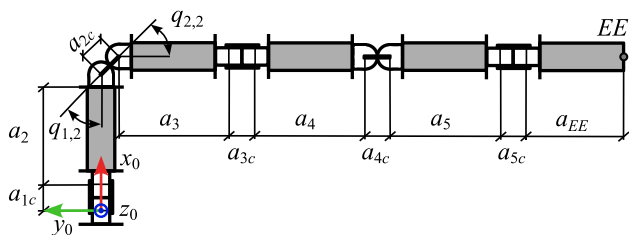
Fig. 4 Robot configuration corresponding to maximum torsional load on the first joint, M_t

Fig. 5 3D CAD model of the simplified joint highlighting the point P

– The joint geometry is simplified considering the bodies most sensitive to M_t, i.e. the intermediate links connected by two shafts;
– All the contact interfaces are assumed to be bonded;
– P-elements polynomial order from minimum 3 to maximum 9;
– Mesh element type tetrahedron;
– Mesh element edge size 5 mm;
– Multi-Pass Adaptive method with percent convergence 10 %.

All the mechanical components considered in this study are made of aluminium alloy A7075 T6, also known as Ergal. This material has been chosen because performs well in terms of mechanical stiffness-to-weight ratio:

$$\frac{E}{\rho} = 26 \ \frac{\text{MPa m}^3}{\text{kg}},$$

where E is the Young modulus and ρ is the density. Such value is comparable to that of titanium. The physical and mechanical properties are reported in Table 3. The 3D Computer-Aided Design (CAD) model of the simplified joint, whose mass is $m_0 = 0.368$ kg, is reported in Fig. 5.

A first structural static analysis has been performed on the simplified joint where the load M_t is applied on the contact surfaces between the outer shaft and the intermediate links, having constrained the inner shaft. Figure 6 reports the results of the analysis.

The displacement of the point P, which is one of the end points of the axis of the outer shaft, is

$$u_{P_0} = 0.48 \text{ mm}.$$

Table 3 Physical and mechanical properties of A7075 T6 (Ergal)

Parameter	Symbol	Value	Unit
Density	ρ	2810	kg/m^3
Young modulus	E	71.7	GPa
Poisson ratio	ν	0.33	

The corresponding torsional deformation results in a rotation of

$$\theta_{P_0} = \text{asin}\left(\frac{2u_{P_0}}{l_s}\right) = 10.7 \times 10^{-3} \text{ rad},$$

where $l_s = 90$ mm is the length of the outer shaft. Considering the joints configuration of the robotic system for which the torsional load on the first joint is M_t, the maximum displacement of the position of the end-effector induced by θ_{P_0} is

$$u_{EE_0} = 20.9 \text{ mm}.$$

To increase the torsional stiffness of the joint without changing the original geometry of the components, it is necessary to add a stiffener element. Such an element must satisfy the constraints of the geometry of the whole joint, including the gears, the flanges, and the cables. Figures 7b and 8b report the geometrical parameters required to describe such constraints. In the following, two different designs that satisfy such constraints are investigated.

3.1 Tube-shaped geometry

Assuming a ring section, with width and thickness w and t, respectively, drawn in the space between the two gears of the joint as shown in Fig. 7a, the relations represented in Fig. 7b
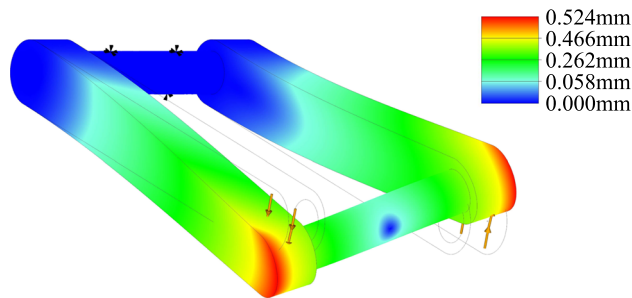
Fig. 6 Deformed model of the simplified joint showing the constraint on the inner shaft and the torsional load on the outer shaft. A scale factor of 10 is applied to better visualise the deformation
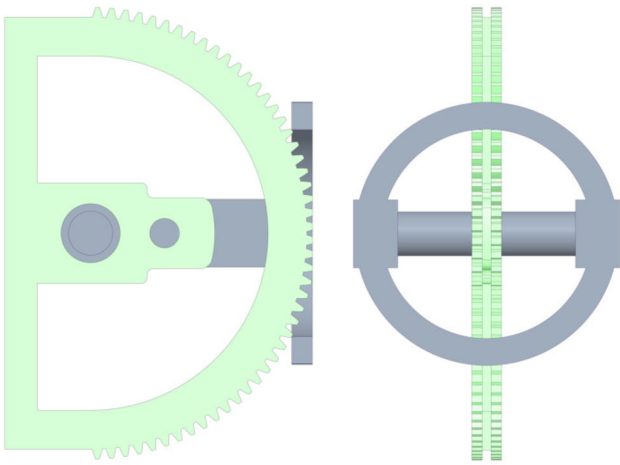
(a) Lateral and middle cross-section of a stiffener element surrounding the gears.
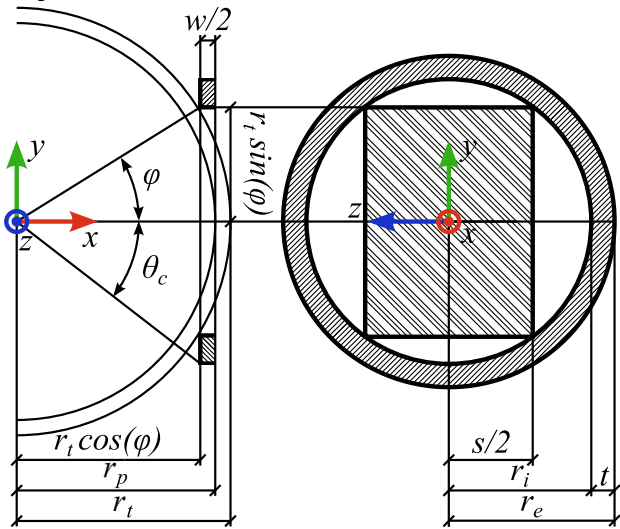
(b) Geometrical parameters for a stiffener element surrounding the gears (not to scale).

Fig. 7 Geometrical constraints of solution 1

are defined:

$$\varphi = \mathrm{acos}\left(\frac{2r_p - w}{2r_t}\right),$$

$$r_i = \sqrt{\left(\frac{s}{2}\right)^2 + [r_t \sin(\varphi)]^2},$$

$$t = r_e - r_i = \left[\frac{d\cos(q_m) - d_c}{2}\right] + \qquad (9)$$

$$- \sqrt{\left(\frac{s}{2}\right)^2 + r_t^2\left[1 - \left(\frac{2r_p - w}{2r_t}\right)^2\right]},$$

where r_t and r_p are the tip and the pitch radii of the gear, respectively, s is the gear depth, d_c is the cable diameter, and

r_e is the semi-minor axis of the ellipse passing through the positions of the cables when $q_1 = q_m$.

Considering a minimum thickness t_{min} and a minimum width w_{min}, w lies in the range $[w_{min}, w_{max}]$ where

$$w_{max} = w(t_{min}).$$

The values of the geometric parameters required to describe the constraints that the tube-shaped geometry has to satisfy are listed in Table 4.

Furthermore, assuming a support similar in shape to a cylindrical tube with the ring cross-section described above, its faces must be cut to avoid contact between the support and the joint flanges. As shown in Fig. 7b, the cut angle θ_c is subject to the following constraint:

$$\theta_c = \mathrm{atan2}\left(r_e, r_p - \frac{w}{2}\right) < q_m.$$

Given the limits of w, it is trivial to prove that such a condition is always respected.

3.2 Rectangular-shaped geometry

Assuming two equal rectangular sections, with base and height b and h, respectively, drawn in the inner spaces of both the gears of the joint as shown in Fig. 8a, the relations represented in Fig. 8b are defined:

$$h = 2\sqrt{r_2^2 - (r_1 + b)^2}, \qquad (10)$$

where r_2 is the inner radius of the gear and r_1 is the radius of the circle tangent to the mounting support placed inside the gear.
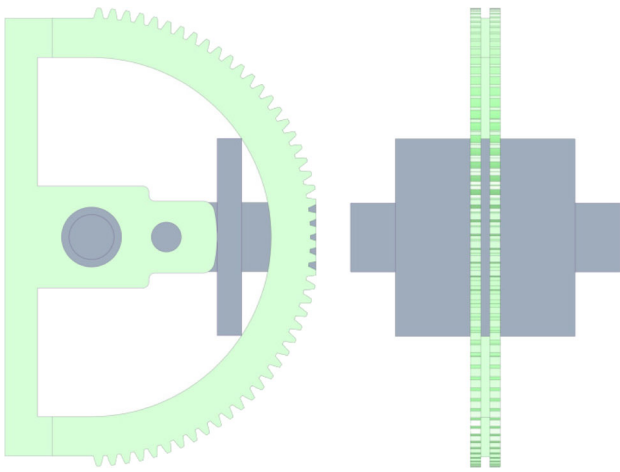
Assuming a minimum height h_{min}, h lies in the range $[h_{min}, h_{max}]$, with

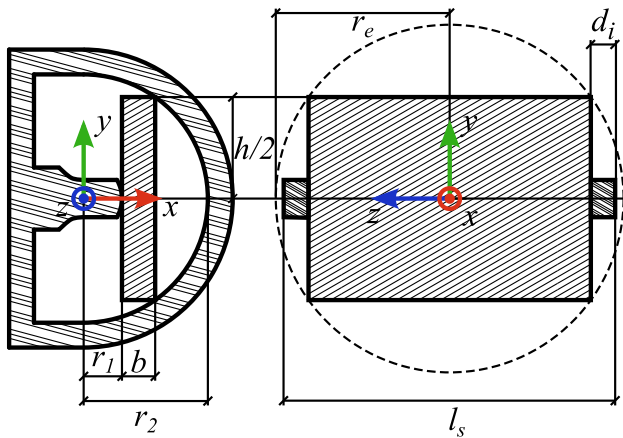$$h_{max} = 2\sqrt{r_e^2 - \left(\frac{l_s - 2d_i}{2}\right)^2},$$

Table 4 Geometric parameters describing the tube-shaped geometry constraints

Parameter	Value	Unit
d	130	mm
r_t	76.5	mm
r_p	75	mm
s	10	mm
d_c	3	mm
r_e	44.5	mm
t_{min}	1	mm
w_{min}	1	mm
w_{max}	23.7	mm

(a) Lateral and middle cross-section of a stiffener element mounted in the inner space of the gears.

(b) Geometrical parameters for a stiffener element mounted in the inner space of the gears (not to scale).

Fig. 8 Geometrical constraints of solution 2

where d_i is the depth of the intermediate link. The base b belongs in $[b_{min}, b_{max}]$, with

$$b_{min} = b(h_{max}),$$
$$b_{max} = b(h_{min}).$$

Table 5 Geometric parameters describing the rectangular-shaped geometry constraints

Parameter	Value	Unit
r_1	42	mm
r_2	60	mm
d_i	15	mm
h_{min}	1	mm
h_{max}	65.7	mm
b_{min}	8.2	mm
b_{max}	17.998	mm
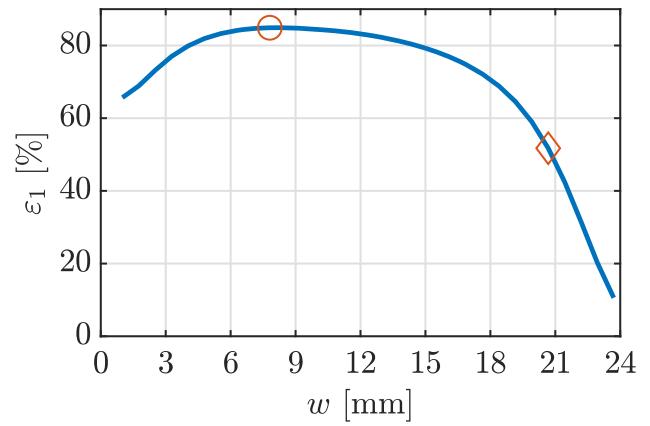
Fig. 9 Sensitivity analysis for solution 1 in terms of ε. The orange circle highlights the values associated with maximum efficacy

The values of the geometric parameters required to describe the constraints that the rectangular-shaped geometry has to satisfy are listed in Table 5.

4 Proposed solutions

The displacement u_{P_0} can be reduced by increasing the torsional stiffness of the joint adding a stiffener that connects the two intermediate links. To compare different stiffener designs, the following performance indicators are evaluated for a given i^{th} solution:

– the efficacy ε_i is calculated as follows

$$\varepsilon_i = 100 \frac{\left(u_{P_0} - u_{P_i}\right)}{\left(u_{P_0}\right)},$$
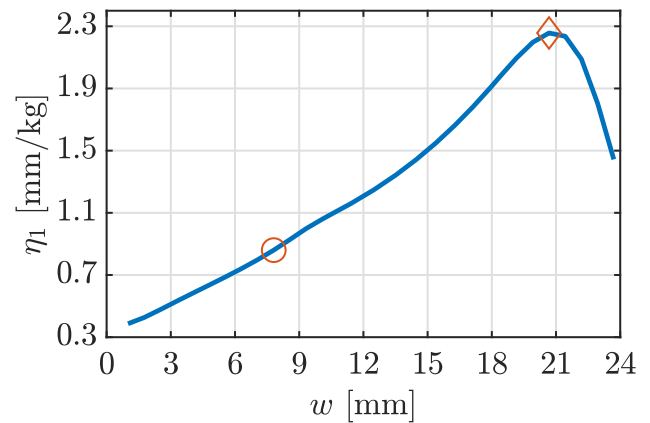

Fig. 10 Sensitivity analysis for solution 1 in terms of η. The orange diamond highlights the values associated with maximum efficiency
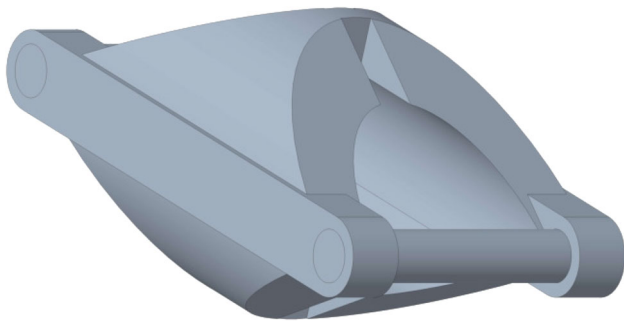
Fig. 11 Design for solution 1 that maximises ε_1

Fig. 13 Deformed model of the simplified joint with the stiffener solution 1 that maximises ε. A scale factor of 10 is applied to better visualise the deformation

where u_{P_i} is the displacement of the point P with the stiffener, defined as the percentage reduction of the displacement with respect to the joint without the stiffener;
– the efficiency η_i is calculated as follows

$$\eta_i = \frac{\left(u_{P_0} - u_{P_i}\right)}{(m_i - m_0)},$$

where m_i is the mass of the joint with the stiffener.

According to the geometrical constraints, assumptions, and parameters introduced in Section 3, two different solutions have been designed and analysed.

4.1 Solution 1: tube-shaped stiffener

The first proposed solution is a tube-shaped stiffener surrounding the gears. This element is obtained from a cylindrical tube with length $2r_p$, external radius r_e, and thickness t, whose faces are cut each by two planes tilted of the angle θ_c. In addition, two portions of material with a rectangular cross-section in the x-z plane are removed to avoid interference between the stiffener element and the gears, maintaining a width of w according to Eq. 9. A sensitivity analysis has been performed varying the parameter w within the range $[w_{\min}, w_{\max}]$ with 30 steps. The correspond-
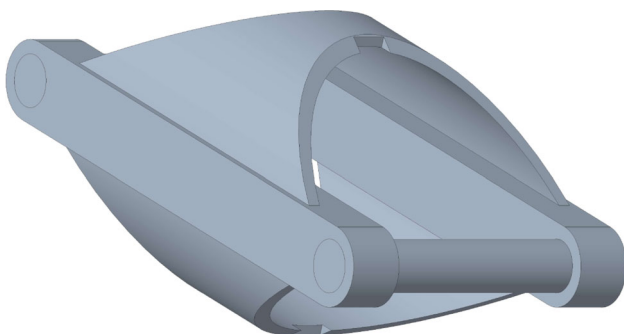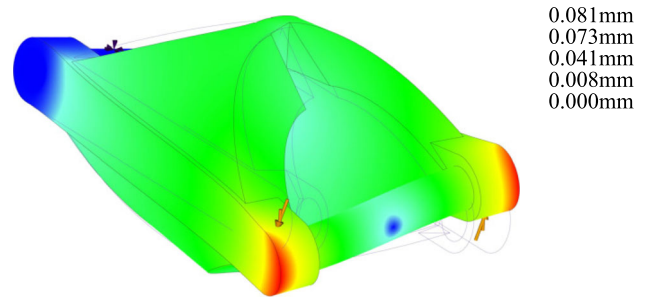
ing results in terms of performance indicators are reported in Figs. 9 and 10.

Two structural static analyses have been performed with the designs corresponding to the parameters that maximise ε_1 and η_1. The two designs are depicted in Figs. 11 and 12.

The corresponding structural static analyses are shown in Figs. 13 and 14.

4.2 Solution 2: rectangular-shaped stiffener

The second proposed solution comprises a pair of rectangular-shaped stiffeners passing through the gears. Both elements have a rectangular cross-section with base b and height h, which are related by Eq. 10. A sensitivity analysis has been performed varying the parameter b within the range $[b_{\min}, b_{\max}]$ with 30 steps. The corresponding results in terms of performance indicators are reported in Figs. 15 and 16.

Two structural static analyses have been performed with the designs corresponding to the parameters that maximise ε_2 and η_2. The two designs are depicted in Figs. 17 and 18.

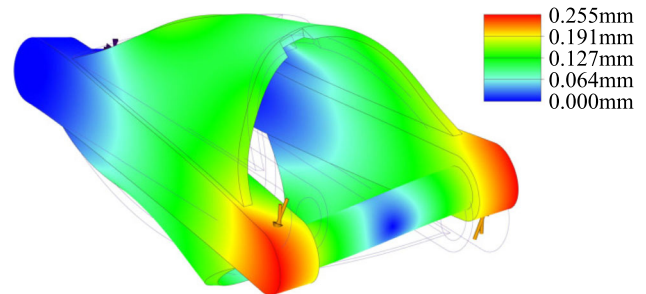The corresponding structural static analyses are shown in Figs. 19 and 20.

Fig. 12 Design for solution 1 that maximises η_1

Fig. 14 Deformed model of the simplified joint with the stiffener solution 1 that maximises η. A scale factor of 10 is applied to better visualise the deformation
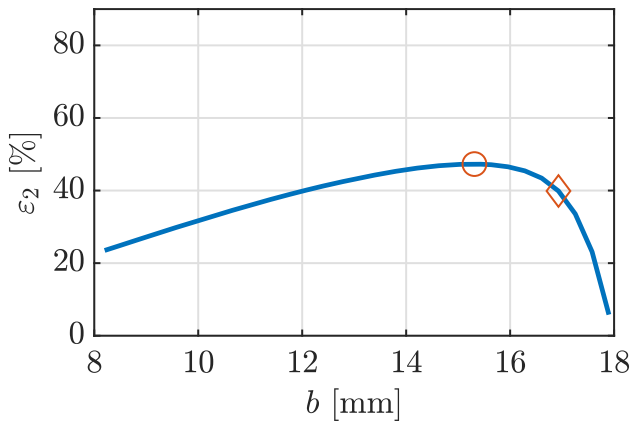
Fig. 15 Sensitivity analysis for solution 2 in terms of ε. The orange circle highlights the values associated with maximum efficacy
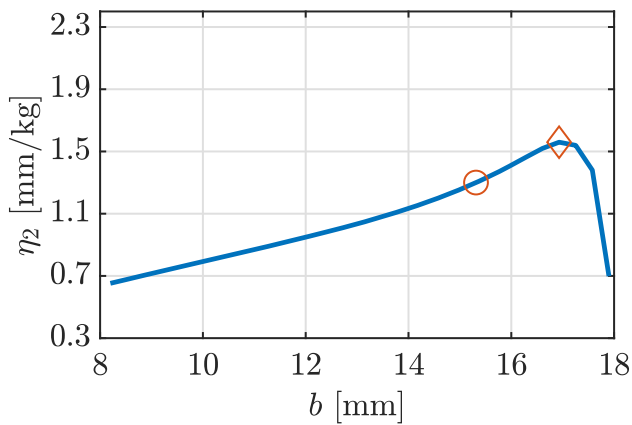

Fig. 16 Sensitivity analysis for solution 2 in terms of η. The orange diamond highlights the values associated with maximum efficiency
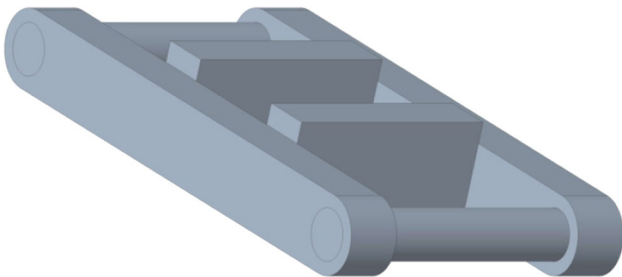

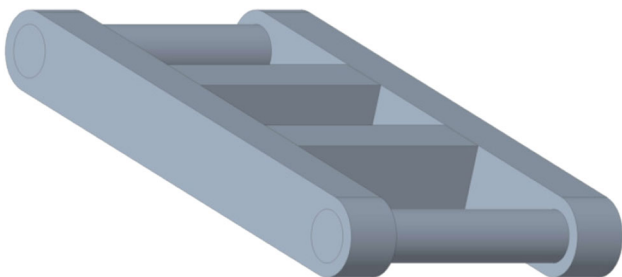**Fig. 17** Design for solution 2 that maximises ε_2

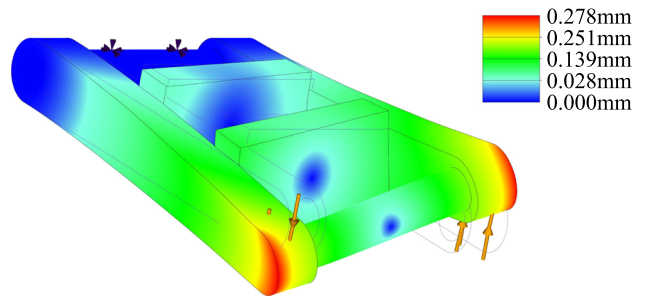**Fig. 18** Design for solution 2 that maximises η_2

Fig. 19 Deformed model of the simplified joint with the stiffener solution 2 that maximises ε. A scale factor of 10 is applied to better visualise the deformation
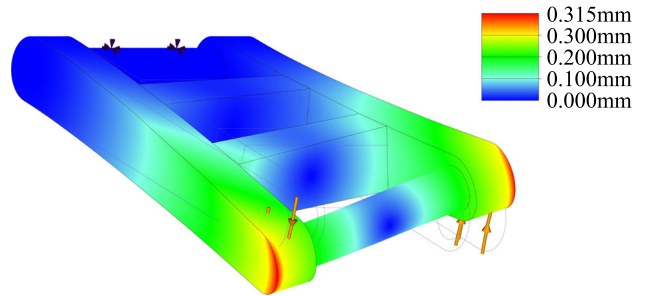

Fig. 20 Deformed model of the simplified joint with the stiffener solution 2 that maximises η. A scale factor of 10 is applied to better visualise the deformation

Table 6 Summary of the results of the sensitivity analyses for solution 1 and 2

Solution 1	w [mm]	m_1 [kg]	ε_1 [%]	η_1 [mm/kg]
ε_{max}	7.8	0.843	84.9	0.9
η_{max}	20.7	0.478	51.7	2.3
Solution 2	b [mm]	m_2 [kg]	ε_2 [%]	η_2 [mm/kg]
ε_{max}	15.3	0.543	47.3	1.3
η_{max}	16.9	0.491	39.9	1.6

Table 7 End-effector displacement corresponding to the first joint without stiffener and the first joint with solution 1 and 2 for ε_{max} and η_{max}

		u_P [mm]	θ_P $[\times 10^{-3}\text{rad}]$	u_{EE} [mm]
Without stiffener		0.481	10.7	20.9
Solution 1	ε_{max}	0.073	1.6	3.2
	η_{max}	0.232	5.2	10.1
Solution 2	ε_{max}	0.254	5.6	11.0
	η_{max}	0.289	6.4	12.6

4.3 Results and discussion

Figures 9, 10, 15 and 16 report the sensitivity analyses for solution 1 and 2, respectively, in terms of ε and η. Table 6 summarises the corresponding results.

Solution 1 performs better in both performance indicators. Furthermore, in the range of w between the points of maximum efficacy (orange circle) and maximum efficiency (orange diamond), ε_1 and η_1 are monotonically decreasing and increasing, respectively. Since, in this range, the absolute local slope of ε_1 is much lower than that of η_1, it is possible to have a slight loss in efficacy (i.e. less displacement reduction) while retaining high performance in efficiency (i.e. less mass added). Consequently, different stiffener designs can suit the different joints of the robot depending on the magnitude of the torsional load that affects the joint itself. In addition, the displacement on the end-effector has been evaluated considering the robotic system in the configuration depicted in Fig. 4 and mounting the two proposed stiffener on the first joint. Table 7 reports the comparison of the two displacements on the end-effector for both solutions with respect to the joint without stiffener.

Solution 1 performs better also in terms of positioning accuracy of the end-effector. Furthermore, the proposed design for solution 1 can be easily manufactured starting from a cylindrical tube. Finally, this element can be mounted on the gear transmission joint without changing the assembly procedure so far defined. Figures 21 and 22 show the assembled simplified model of the joint for solutions 1 and 2, respectively.
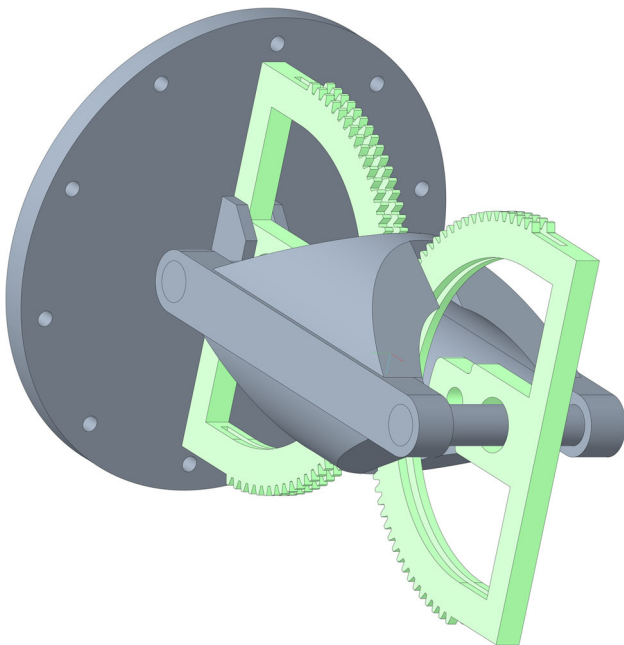

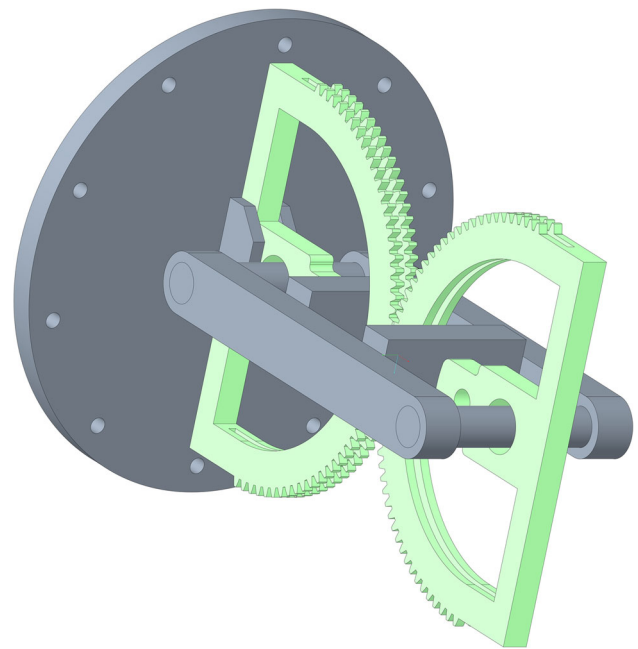**Fig. 21** 3D CAD model of the joint with the solution 1

Fig. 22 3D CAD model of the joint with the solution 2

5 Conclusion

This paper presents two designs for increasing the torsional stiffness of a gear transmission joint of a fully actuated cable-driven hyper-redundant robot. First, a summary of the fully actuated cable-driven hyper-redundant robot and a description of the joint are reported. Then, the critical aspects of the mechanical system are highlighted and the geometrical constraints the possible stiffener solutions have to satisfy are defined. Subsequently, a tube-shaped and a rectangular-shaped stiffeners are introduced. Exploiting the geometrical constraints, a single independent variable defines the whole geometry of the stiffeners. Performing a sensitivity finite elements analysis by varying such independent variables, the performance of the two solutions is compared in terms of added mass and displacement reduction. The tube-shaped stiffener provides a more significant displacement reduction while adding less mass. In addition, in a wide range of the independent variable, the displacement reduction and the added mass are anti-correlated. Consequently, different tube-shaped designs can suit the different joints of the robot depending on the magnitude of the torsional load that affects the joint itself. Moreover, the effect that the tube-shaped design has on the end-effector positioning accuracy is greater than that of the rectangular-shaped one. Finally, the proposed tube-shaped design can be easily manufactured and mounted.

Future works will include the stress analysis to perform a multi-parameters optimisation of the tube-shaped stiffener to obtain a uniform design removing the material that do not transfer loads at the supports further reducing the mass

and displacement. Next, a physical prototype of the fully actuated cable-driven hyper-redundant robot implementing the proposed stiffener will be developed and tested to verify its performance. Furthermore, a significant improvement could be obtained by employing the generative design combined with the additive manufacturing technology to develop a miniature polymeric version of the prototype.

Declarations

Competing interests The authors declare no competing interests.

References

1. Luk BL, Liu K, Collie AA, Cooke DS, Chen S (2006) Tele-operated climbing and mobile service robots for remote inspection and maintenance in nuclear industry. Ind Robot Int J

2. Holland J, Kingston L, McCarthy C, Armstrong E, O'Dwyer P, Merz F, McConnell M (2021) Service robots in the healthcare sector. Robotics 10(1):47

3. Wirtz J, Patterson PG, Kunz WH, Gruber T, Lu VN, Paluch S, Martins A (2018) Brave new world: service robots in the frontline. J Serv Manag 29(5):907–931

4. Robotics S (2016) Robotics 2020 multi-annual roadmap for robotics in Europe. SPARC Robotics, EU-Robotics AISBL, The Hauge, The Netherlands, accessed 2023/03/01

5. Zhuang F, Zupan C, Chao Z, Yanzheng Z (2008) A cable-tunnel inspecting robot for dangerous environment. Int J Adv Robot Syst 5(3):32

6. Alhassan AB, Zhang X, Shen H, Xu H (2020) Power transmission line inspection robots: a review, trends and challenges for future research. Int J Electr Power Energy Syst 118

7. Tur JMM, Garthwaite W (2010) Robotic devices for water main in-pipe inspection: a survey. J Field Robot 4(27):491–508

8. Yu L, Yang E, Ren P, Luo C, Dobie G, Gu D, Yan X (2019) Inspection robots in oil and gas industry: a review of current solutions and future trends. In: 2019 25th International Conference on Automation and Computing (ICAC), IEEE, pp 1–6

9. Lim RS, La HM, Shan Z, Sheng W (2011) Developing a crack inspection robot for bridge maintenance. In: 2011 IEEE international conference on robotics and automation, IEEE, pp 6288–6293

10. SKF (2019) Robotics for infrastructure inspection and maintenance network. https://rimanetwork.eu/about-rima. Accessed 02 Feb 2023

11. Bellicoso CD, Bjelonic M, Wellhausen L, Holtmann K, Günther F, Tranzatto M, Fankhauser P, Hutter M (2018) Advances in real-world applications for legged robots. J Field Robot 35(8):1311–1326

12. Nooralishahi P, Ibarra-Castanedo C, Deane S, López F, Pant S, Genest M, Avdelidis NP, Maldague XP (2021) Drone-based non-destructive inspection of industrial sites: a review and case studies. Drones 5(4):106

13. Cieślak R, Morecki A (1999) Elephant trunk type elastic manipulator-a tool for bulk and liquid materials transportation. Robotica 17(1):11–16

14. Hannan MW, Walker ID (2000) Analysis and initial experiments for a novel elephant's trunk robot. In: Proceedings. 2000 IEEE/RSJ international conference on intelligent robots and systems (IROS 2000)(Cat. No. 00CH37113), vol 1, IEEE, pp 330–337

15. Pistone A, Canali C, Gloriani C, Leggieri S, Guardiani P, Caldwell D (2019) Reconfigurable inspection robot for industrial applications. Procedia Manuf 38:597–604

16. Guglielmino E, Tsagarakis N, Caldwell DG (2010) An octopus anatomy-inspired robotic arm. In: 2010 IEEE/RSJ international conference on intelligent robots and systems, IEEE, pp 3091–3096

17. Canali C, Pistone A, Ludovico D, Guardiani P, Gagliardi R, Dal Verme LDMC, Sofia G, Caldwell DG (2022) Design of a novel long-reach cable-driven hyper-redundant snake-like manipulator for inspection and maintenance. Appl Sci (Switzerland) 12(7)

18. Buckingham R, Chitrakaran V, Conkie R, Ferguson G, Graham A, Lazell A, Lichon M, Parry N, Pollard F, Kayani A et al (2007) Snake-arm robots: a new approach to aircraft assembly. Tech Rep, SAE Technical Paper

19. Perrot Y, Gargiulo L, Houry M, Kammerer N, Keller D, Measson Y, Piolain G, Verney A (2012) Long-reach articulated robots for inspection and mini-invasive interventions in hazardous environments: recent robotics research, qualification testing, and tool developments. J Field Robot 29(1):175–185

20. Endo G, Horigome A, Takata A (2019) Super dragon: a 10-m-long-coupled tendon-driven articulated manipulator. IEEE Robot Autom Lett 4(2):934–941

21. Mitsui T, Morigaki Y, Cole M, Martin S, Rood M, Masaki H, Dekura T (2017) Long reach manipulator for PCV repair at Fukushima Daiichi-17082. In: WM2017 Conference, March

22. Tokyo Electric Power Company Holdings I (2020) Status of r&d for the trial removal of fuel debris from unit 2. Accessed 15 Sept 2022

23. Guardiani P, Ludovico D, Pistone A, Abidi H, Zaplana I, Lee J, Caldwell DG, Canali C (2022) Design and analysis of a fully actuated cable-driven joint for hyper-redundant robots with optimal cable routing. J Mech Robot 14(2)

24. Rivin EI (1987) Mechanical design of robots. McGraw-Hill, Inc

25. Rivin E (1999) Stiffness and damping in mechanical design. CRC Press

26. Acanfora V, Sellitto A, Fittipaldi F, Riccio A (2022) A feasibility study on innovative reinforced modular frames for automotive applications. In: Macromolecular symposia, vol 404, Wiley Online Library, pp 2100455

27. Xu N, Sun C, Wang X (2021) Parametric modeling and structure optimization technology of automobile twist beam. In: Proceedings of China SAE congress 2019: Selected Papers, Springer, pp 169–176

28. Briard T, Segonds F, Zamariola N (2020) G-DfAM: a methodological proposal of generative design for additive manufacturing in the automotive industry. International Journal on Interactive Design and Manufacturing (IJIDeM) 14(3):875–886

29. Lianos AK, Koutsoukos S, Bikas H, Stavropoulos P (2020) Manufacturability assessment and design for am. Procedia CIRP 91:290–294

30. Khalil W, Dombre E (2004) Modeling, identification and control of robots. Butterworth-Heinemann
31. Willis R (1870) Principles of mechanism. Longmans, Green

Authors and Affiliations

Ardit Poka[1,2] · Federico Manara[1,2] · Daniele Ludovico[1] · Alessandro Pistone[1] · Lorenzo De Mari Casareto Dal Verme[1,3] · Giovanni Berselli[1,2] · Darwin G. Caldwell[1] · Carlo Canali[1]

Federico Manara
federico.manara@iit.it

Daniele Ludovico
daniele.ludovico@iit.it

Alessandro Pistone
alessandro.pistone@iit.it

Lorenzo De Mari Casareto Dal Verme
lorenzo.demaricasareto@iit.it

Giovanni Berselli
giovanni.berselli@unige.it

Darwin G. Caldwell
darwin.caldwell@iit.it

Carlo Canali
carlo.canali@iit.it

[1] Advanced Robotics (ADVR), Italian Institute of Technology, Genoa, Italy

[2] Department of Mechanical, Energy, Management and Transportation Engineering (DIME), University of Genova, Genova, Italy

[3] Department of Computer Science, Bioengineering, Robotics and Systems Engineering (DIBRIS), University of Genova, Genova, Italy